

# Sub-megahertz homogeneous linewidth for Er in Si via in situ single photon detection

Ian R. Berkman,<sup>1,\*</sup> Alexey Lyasota,<sup>1</sup> Gabriele G. de Boo,<sup>1</sup> John G. Bartholomew,<sup>2,3</sup> Brett C. Johnson,<sup>4,5</sup> Jeffrey C. McCallum,<sup>4</sup> Bin-Bin Xu,<sup>1</sup> Shouyi Xie,<sup>1</sup> Rose L. Ahlefeldt,<sup>6</sup> Matthew J. Sellars,<sup>6</sup> Chunming Yin,<sup>1,7</sup> and Sven Rogge<sup>1</sup>

<sup>1</sup>*Centre of Excellence for Quantum Computation and Communication Technology, School of Physics, University of New South Wales, Sydney, NSW 2052, Australia*

<sup>2</sup>*Centre for Engineered Quantum Systems, School of Physics, The University of Sydney, Sydney, NSW 2006, Australia*

<sup>3</sup>*The University of Sydney Nano Institute, The University of Sydney, Sydney, NSW 2006, Australia*

<sup>4</sup>*Centre of Excellence for Quantum Computation and Communication Technology, School of Physics, University of Melbourne, Victoria 3010, Australia*

<sup>5</sup>*Centre of Excellence for Quantum Computation and Communication Technology, School of Engineering, RMIT University, Victoria 3001, Australia*

<sup>6</sup>*Centre of Excellence for Quantum Computation and Communication Technology, Research School of Physics, Australian National University, Canberra, ACT 0200, Australia*

<sup>7</sup>*Hefei National Laboratory for Physical Sciences at the Microscale, CAS Key Laboratory of Microscale Magnetic Resonance and School of Physical Sciences, University of Science and Technology of China, Hefei 230026, China*

We studied the optical properties of a resonantly excited trivalent Er ensemble in Si accessed via in situ single photon detection. A novel approach which avoids nanofabrication on the sample is introduced, resulting in a highly efficient detection of 70 excitation frequencies, of which 63 resonances have not been observed in literature. The center frequencies and optical lifetimes of all resonances have been extracted, showing that 5% of the resonances are within 1 GHz of our electrically detected resonances and that the optical lifetimes range from 0.5 ms up to 1.5 ms. We observed inhomogeneous broadening of less than 400 MHz and an upper bound on the homogeneous linewidth of 1.4 MHz and 0.75 MHz for two separate resonances, which is a reduction of more than an order of magnitude observed to date. These narrow optical transition properties show that Er in Si is an excellent candidate for future quantum information and communication applications.

## INTRODUCTION

Rare earth (RE) ions embedded in a host crystal possess numerous interesting properties for quantum information processing. RE ions can have near-lifetime limited coherence times on their optical transitions [1], as long as 4.4 ms [2], and hyperfine coherence times from seconds to hours in carefully controlled magnetic fields [3, 4]. While RE ions have weaker oscillator strengths than other solid state optical emitters, single ion readout has been achieved in a multiple of host crystals such as YAlO<sub>3</sub>[5, 6], YVO<sub>4</sub>[7], Y<sub>2</sub>SiO<sub>5</sub>[8–10] and Si [11]. These properties make RE ions in solid state hosts excellent material for quantum memories[3, 12] and potential candidates for future qubits [13].

The RE ion Er in solids most commonly has a <sup>4</sup>I<sub>15/2</sub> ground state and a <sup>4</sup>I<sub>13/2</sub> excited state [14]. The optical transition from the lowest crystal field level of <sup>4</sup>I<sub>15/2</sub> ground state to the lowest lying level of the <sup>4</sup>I<sub>13/2</sub> excited state occurs at approximately 1540 nm, hence within the technologically important telecom C-band. This convenient wavelength makes Er particularly attractive for quantum communication applications, as Er-based devices will be telecom-compatible.

Incorporating Er into Si, by means such as ion implantation or chemical vapour deposition, allows integration

into standard complementary metal-oxide-semiconductor processing and provides the ability to fabricate nanophotonic structures [15]. Furthermore, Si can be enriched to less than 1 ppm <sup>29</sup>Si, effectively resulting in a low magnetic noise environment [16, 17] which leads to linewidths as narrow as 33 MHz for T centers [18] and 5 MHz for the donor-bound excitons [19] in silicon.

## RESONANT PHOTOLUMINESCENCE EXCITATION SPECTROSCOPY

Er in Si is able to occupy multiple classes of sites [14, 20], however most of the sites essential for quantum information have not been characterized thus far. The three main methods used to identify these Er:Si sites are namely electron paramagnetic resonance (EPR), photoluminescence (PL) and photoluminescence excitation (PLE).

Methods utilizing EPR rely on microwaves to probe the paramagnetic properties of electrons in closely separated levels within the <sup>4</sup>I<sub>15/2</sub> state. However, the use of microwaves makes it impossible to excite from the <sup>4</sup>I<sub>15/2</sub> ground state to the <sup>4</sup>I<sub>13/2</sub> excited state. Both PL and PLE address these energy levels by using photon excitation. In a PL experiment, above-bandgap light is used to excite the Er ions and the photoluminescence is recorded using a spectrometer. The spectrum includes decay from the lowest <sup>4</sup>I<sub>13/2</sub> to the multiple <sup>4</sup>I<sub>15/2</sub> levels following the

\* i.berkman@unsw.edu.au

excitation of the Si host [20], where the intensity depends on the excitation transfer efficiency from the Si [21]. The crystal field levels in the excited  $^4I_{13/2}$  state are inaccessible in PL, but obtainable in PLE when using a narrow band laser to resonantly excite the population into multiple  $^4I_{13/2}$  levels and collect the photoluminescence. In addition, less free carriers are generated that can affect the spectrum and lifetime [22]. Differences of exciting resonantly or using above-band gap excitation have been observed in Er-doped GaAs where Er centers that exhibited photoluminescence only under direct 4f-shell excitation did not show photoluminescence under above-band gap excitation [23], thus corroborating the significance of PLE for investigating photoluminescent Er sites and the corresponding  $^4I_{13/2}$  crystal field levels in semiconductors.

Recent PLE experiments in Er:Si have shown nine narrow photoluminescence resonances associated with different Er sites and potentially different crystal field levels of these sites [24]. Our measurement of a higher density sample observed 7 of the previously detected resonances, marked by the † in Table AI, and characterized 63 additional resonances.

## Experiment

In our experiment we collected the emission of  $\text{Er}^{3+}$  ions in an  $1.7\text{ mm} \times 1.7\text{ mm}$  Si chip following resonant excitation with a laser. The chip was diced from a  $300\text{ }\mu\text{m}$  thick double-side-polished Si wafer containing a background doping of P ranging between  $0.9 \times 10^{15}\text{ cm}^{-3}$  to  $5 \times 10^{15}\text{ cm}^{-3}$ . To study the optical transitions without the complication of hyperfine splitting, the nuclear spin-free  $^{170}\text{Er}$  isotope was implanted with multiple ion energies and fluences into one side of the chip to form a constant concentration profile of  $1 \times 10^{18}\text{ cm}^{-3}$  over a depth of  $0.2\text{ }\mu\text{m}$  to  $0.6\text{ }\mu\text{m}$ . The Er concentration of the sample is an order of magnitude higher than the concentration used in our electrical detection experiments [11, 25] to potentially increase the probability of detecting photoluminescence. In PL experiments, co-implanting Er with O increases the photoluminescence [26, 27] and leads to sharp lines in EPR spectroscopy [28]. Hence, O was likewise implanted with multiple energies to create an overlapping profile but with a concentration of  $1 \times 10^{19}\text{ cm}^{-3}$ . Following implantation, the chip was annealed at  $700\text{ }^\circ\text{C}$  for 10 min in an  $\text{N}_2$  atmosphere, which has resulted in optically active Er ions in silicon [11, 15]. Afterwards, a  $190\text{ nm}$  thick  $\text{SiN}_x$  anti-reflective coating on both sides was formed using plasma-enhanced chemical vapor deposition to reduce Fabry-Pérot oscillations and enhance the optical transmission through the Si.

The implanted side was placed against the top of a WSi-based, optical cavity-embedded superconducting single photon detector (SSPD) [Supplemental Material S-A]. SSPDs are able to detect single photons with high efficiency in a wide spectral range from  $250\text{ nm}$  [29] up

to  $7\text{ }\mu\text{m}$  [30–32]. By adjusting the thickness of the optical cavity, the absorption can be tailored to a desired wavelength. We fabricated an SSPD with a peak system detection efficiency of 66.27% at  $1550\text{ nm}$  including a bandwidth of approximately  $\pm 50\text{ nm}$  for the measurement.

The chip was sandwiched between the SSPD and an optical fiber that had its core aligned with the SSPD. The latter allowed an optical excitation of Er ions in direct proximity to the SSPD. The optical mode waist resulted in a tightly focused excitation spot at the Er rich sample plane of  $20\text{ }\mu\text{m}$ , equal to the working area of the SSPD. The experiment was operated at  $300\text{ mK}$  to ensure a low dark count rate on the SSPD. Moreover, this temperature is low enough to minimize non-radiative recombination of the Er [22, 33, 34].

To excite the Er ions, we used a semiconductor diode laser (Pure Photonics PPCL550) with an output pulse modulated by two acousto-optical modulators (AOMs) connected in series, resulting in an extinction ratio greater than 100 dB. After the excitation pulse, we recorded the number of counts from the SSPD with a digital counter (Keysight 53131A or National Instruments PCI-6602).

## Broad spectral survey

The resonant PLE spectrum was obtained by pulsing the laser for  $100\text{ }\mu\text{s}$  and integrating the counts from  $10\text{ }\mu\text{s}$  to  $1\text{ ms}$  after the pulse [Fig. 1]. This was repeated 1000 times at each optical frequency before the excitation laser was stepped to the next optical frequency. In total, the range of  $1516\text{ nm}$  to  $1550\text{ nm}$  has been scanned in steps of  $50\text{ MHz}$  ( $0.4\text{ pm}$ ). The laser line was broadened with a frequency modulation of  $60\text{ MHz}$  in order to avoid stepping over narrow resonances. The laser frequency was monitored at each step with a wavemeter (Bristol 621B).

The spectrum in figure 1 consists of 70 peaks which all displayed a prominence of at least 0.15 counts per pulse, followed a distribution profile and showed an exponential lifetime decay. The excitation wavelength, amplitude, Lorentzian FWHM and optical lifetime of the resonances are listed in the appendix AI and the raw data of the spectrum is provided in the Supplemental Material. These resonances are consistent with different Er sites and may include resonances associated with excitation to higher crystal field levels of the  $^4I_{13/2}$  manifold. Numerous sites could have been activated by the co-implanted O due to the formation of Er-O complexes [14]. The observed resonances had linewidths comparable to Er in other host crystals [35, 36] and can be attributed to different environmental inhomogeneities as well as different sensitivities of the optical transition to these inhomogeneities.

In Fig. 1, the spectrum is compared to the resonantly optically excited, electrically detected resonances of single Er ions [11, 25], indicated by the vertical blue lines, where those excitations were detected via ionization

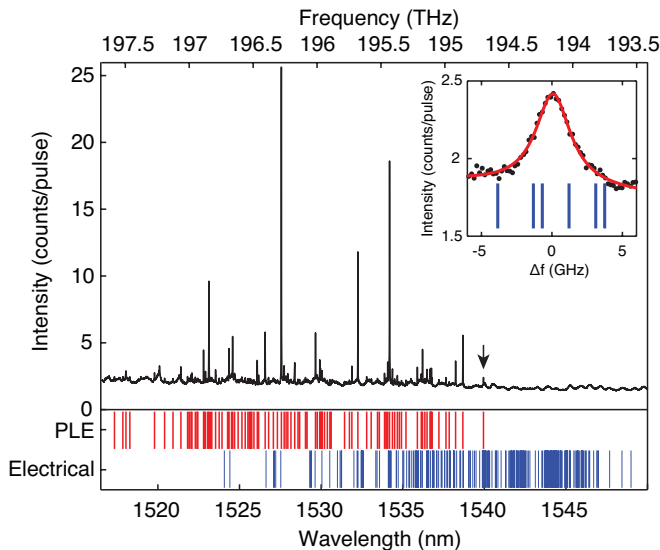


Figure 1. The PLE spectrum compared with the single Er ions found by electrical detection as function of the wavelength measured in vacuum using the wavemeter. The red lines below the plot indicate the center of optically detected resonances and the blue lines indicate the center of electrically detected resonances. Inset: a single optically detected inhomogeneous resonance centered at 1539.948 nm which is fit with a Lorentzian line shape, resolving in a FWHM of 1.5 GHz. The blue lines indicate 6 electrically detected resonances less than 5 GHz away from the centre. The FWHM of the electrically detected resonances are less than 100 MHz.

of a nearby charge trap in a Si fin field-effect transistor (FinFET) device. Electrical detection resulted in numerous detected resonances at longer wavelengths than 1540 nm which are not observed in the PLE spectrum of the current sample. Inherently, optical and electrical detection rely on different decay mechanisms. Optical detection favors sites with a relatively high probability of radiative decay, whereas electrical detection relies on non-radiative decay processes of Er sites. The electrically detected spectrum is the resulting histogram from multiple FinFET devices with varying wavelength scans, different channel dimensions, background doping, Er densities and at temperatures ranging from 20 mK to 4 K. In total, we found 5% of the optically detected PLE resonances are within 1 GHz of the electrically detected resonances, which indicate that they could originate from the same site. This could be confirmed by measuring g-tensors in both sets of sites.

In the next experiment, the splitting of inhomogeneously broadened resonances under an applied magnetic field was studied to understand their site symmetry. The magnetic field was applied perpendicularly to the SSPD and sample, and was limited to 60 mT before the SSPD transitioned from a superconducting to normal state. This caused the SSPD to be incapable of detecting single photons. Under this magnetic field, the resonances presented in following section that showed a narrow spectral

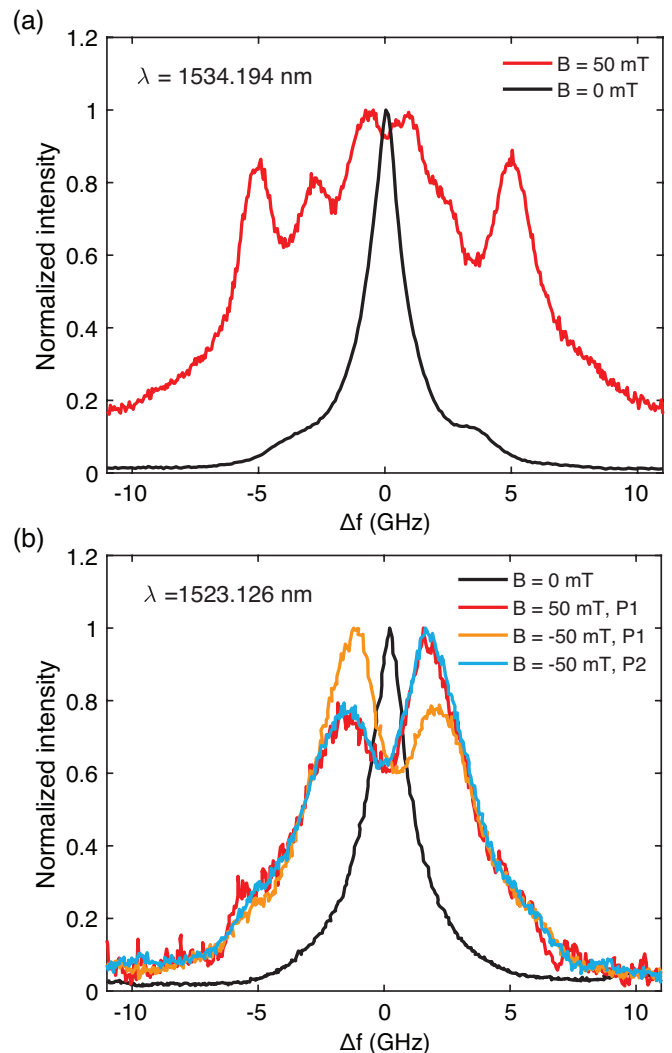


Figure 2. (a) Inhomogeneously broadened resonance at 1534.194 nm at zero field and the splitting into multiple resonances when 50 mT is applied. (b) Inhomogeneously broadened resonance at 1523.126 nm under  $-50$  mT, 0 mT and 50 mT. P1 indicates the polarization which resulted in a maximum intensity of the left peak at  $-50$  mT while P2 indicates the polarization which resulted in a maximum intensity of the right peak at  $-50$  mT.

hole did not split sufficiently, indicating a small g-factor along the direction of the magnetic field.

Two resonances are presented in Fig. 2(a) and Fig. 2(b) which showed different site symmetries. Er ions in sites below cubic symmetry retain a two-fold Kramers' degeneracy in zero field, which is lifted in an applied magnetic field. This in total gives rise to four different possible optical transitions, assuming the g factors in the  $^4I_{15/2}$  and  $^4I_{13/2}$  differ. In the case where Er is located in a site with a point symmetry lower than a cubic symmetry of the Si crystal, the number of magnetically inequivalent subsites can increase up to 24, which corresponds to the  $C_1$  point symmetry. Splitting of an

inhomogeneously broadened resonance into a multiple of well distinguished lines thus confirms that the Er centers reside in well defined crystallographic sites [37].

In Fig. 2(a) a resonance is showed which splits in six lines, which is explained by magnetically inequivalent sites at a lower site symmetry than a cubic symmetry. In Fig. 2(b) a resonance at 1523.199 nm is presented which split in two Zeeman arms with different intensities. The two Zeeman arms were broader than the resonance at zero field, indicating that the remaining two or more lines have not been split sufficiently. The split resonance showed asymmetric peak intensities, which can be attributed to different polarisation dependent oscillator strengths, rather than different Boltzmann populations of the initial states, because the relative intensities of the two peaks can be reversed by rotating the polarisation using a  $\lambda/2$  waveplate. Reversing the magnetic field also reversed the peak intensities, further confirming that the difference is not due to differing Boltzmann populations.

### Homogeneous broadening

The homogeneous linewidth was investigated using transient spectral hole burning [38]. The method relied on the saturation of the fluorescence of an optical transition when the excitation pulse length exceeds the dephasing time due to the saturation of the atomic transition. The optical laser frequency was modulated using an electro-optical modulator (EOM), creating two sidebands 5 GHz apart while suppressing the carrier. The high frequency sideband is centered on the inhomogeneous peak and excites the ensemble for 20  $\mu$ s followed by a 20  $\mu$ s excitation at a detuned laser frequency ( $\Delta f$ ), referred to as the pump and probe pulse respectively. For an equal pump and probe time, the occupation number of the excited state at the end of both pulses is given by

$$\rho_{ee}(2t_p) = \begin{cases} \rho_{res}(2t_p) & \text{for } \Delta f = 0 \\ 2\rho_{res}(t_p)(1 - \frac{1}{2}e^{-t_p/\tau}) & \text{for } \Delta f \gg \gamma_D \end{cases}, \quad (1)$$

where  $t_p$  is the pump time,  $\rho_{res}$  is the occupation number when excited on resonance,  $\tau$  the optical lifetime and  $\gamma_D$  the homogeneous linewidth. The excitation and probe pulse length were chosen to be sufficiently short compared to the optical lifetime resulting in  $\rho_{ee}(2t_{\text{pump}}) \approx 2\rho_{res}(t_{\text{pump}}) > \rho_{res}(2t_{\text{pump}})$  whenever  $\Delta f \gg \gamma_D$ . The repetition time of 3 ms was chosen to be twice the optical lifetime, ensuring the majority of excited Er ions have decayed into the ground states.

To ensure that the off-resonant low frequency sideband did not affect the spectral hole width, the homogeneous broadening was remeasured while the carrier was present. The results present a comparable width when the carrier is present, concluding that hole width is unaffected by the off-resonant light.

Under 360 nW of excitation power, a spectral hole

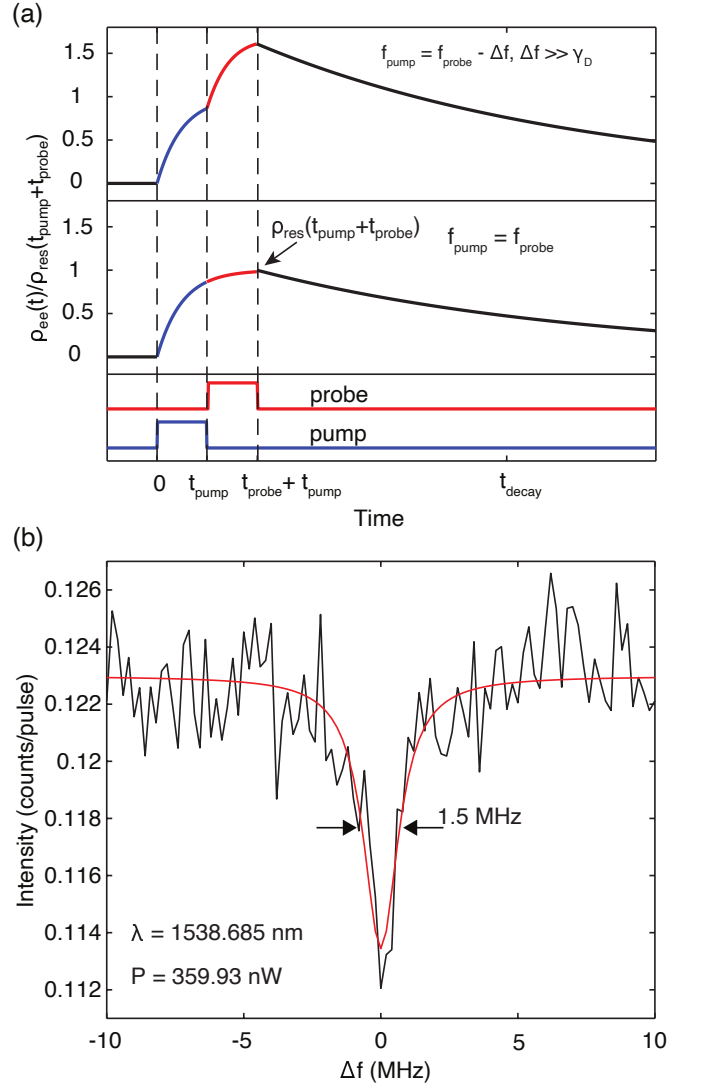


Figure 3. (a) The pulse schematic of the pump and probe microwave sources. The top curve represents the decay signal when the probe frequency is larger than the homogeneous line width. The lower curve represents the decay signal when the probe frequency is equal to the probe frequency, effectively resulting in a pulse of  $2t_{\text{pump}}$  at  $f_{\text{pump}}$  which leads to a reduced decay signal. The curves have been normalized to  $\rho_{res}$  which is the occupation number when the subset is resonantly excited. (b) Upper bound on the homogeneous linewidth at 1538.685 nm. The integrated number of counts up to 1 ms after the probe pulse as function of  $f_{\text{probe}} - f_{\text{pump}}$ . The data is fitted with a Lorentzian distribution, resulting in a FWHM of 1.5 MHz.

was visible at 1538.685 nm and 1532.254 nm. The data is fitted with a Lorentzian distribution resulting in a FWHM of 1.5 MHz [Fig. 3(b)] for 1538.685 nm and 2.8 MHz at 1532.254 nm. The upper bound on the homogeneous linewidth is given by half of the spectral hole linewidth [39], thus leading to a maximum homogeneous linewidth of 0.75 MHz (3.1 neV) and 1.4 MHz (5.8 neV) for 1538.685 nm and 1532.254 nm, respectively.

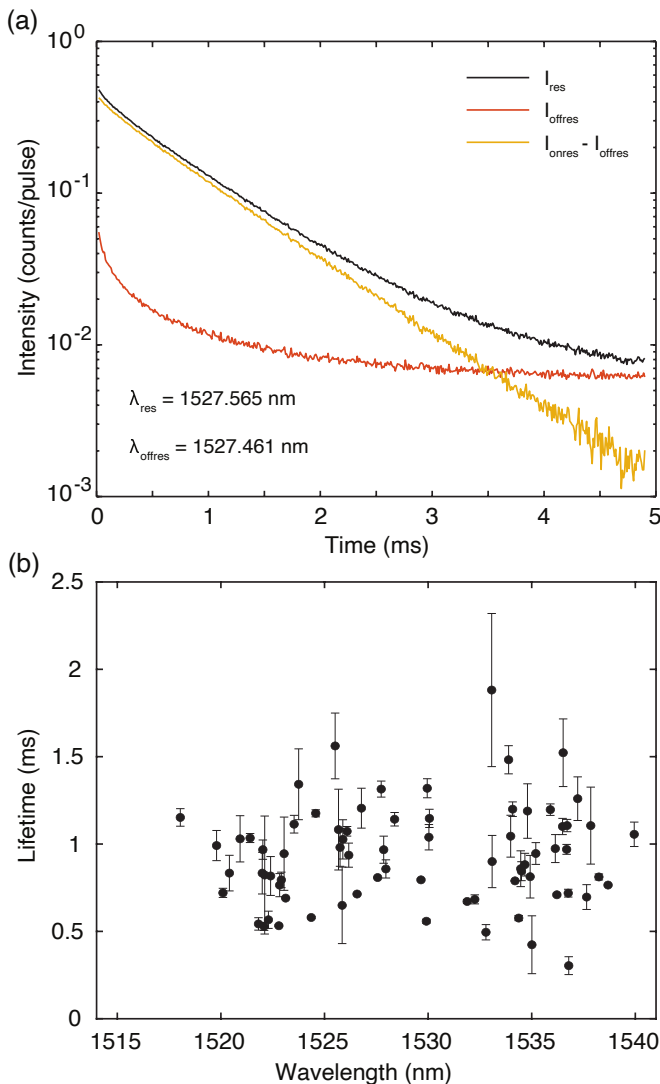


Figure 4. (a) Photoluminescence decay curve for the resonance at 1527.565 nm and the background at 1527.461 nm. (b) Fit result of the lifetime for 70 resonances. Errorbars show the standard error of the fit.

To study the effect of instantaneous spectral diffusion on the spectral hole, the same measurement was carried out using pump and probe widths of 10  $\mu$ s each. The measurement was also repeated with a 90  $\mu$ s delay between the pump and probe width. The choice of delay was limited by the optical lifetime of the resonance, as a longer delay results in a loss of spectral hole visibility. As can be found in Supplemental Material S-E, a delay of 90  $\mu$ s did not affect the hole width and hence instantaneous spectral diffusion does not play a significant role in the spectral hole linewidth on this timescale.

## Lifetime

In the following measurement, the optical lifetime of the 70 resonances was measured. The lifetime of Er varies according to the radiative lifetime of the transition as well as the background doping of silicon [34]. In addition, in this type of fluorescence measurement, the lifetime measured is typically that of the lowest  $^4I_{13/2}$  level, regardless of which crystal field level was excited, because higher crystal field levels rapidly decay non-radiatively to the lowest state [40]. In principle, this means that lines with identical fluorescence lifetimes should be associated with the same site.

To measure the fluorescence lifetime, the number of single photon events was repeatedly recorded for 5 ms after a 100  $\mu$ s excitation pulse centered on the inhomogeneous peak. The signal decay after the excitation pulse did not follow a single exponential curve, but instead was a combination of the resonant signal and a background signal. To separate this background decay, it was measured at an optical frequency where the photoluminescence resonance was absent. It was found to be wavelength independent and consists of a fast ( $\sim 200$   $\mu$ s) and a slow ( $\sim 800$   $\mu$ s) exponential decay [Fig. 4(a)]. This biexponential decay photoluminescence has been observed in other Er:SI systems in the past, in PL experiments [41–44] as well as electroluminescence experiments [22]. These components are related to the radiative decay of excitons and indirectly excited Er ions, respectively. The background is thus attributed to a non-competitive process and can be subtracted from the resonance decay signal. To get a better estimate on the lifetimes, a nearby background decay approximately two times the FWHM at the side was measured at every resonance [Supplemental Material S-D]. The difference between the two followed a single exponential decay for most of the resonances, where the largest amplitude decay trace is shown in Fig. 4(a). A number of resonances show a biexponential decay, marked by \* in Table AI and presented in the Supplemental Material S-D.

A summary of the lifetimes is presented in Table AI. The optical lifetimes ranged from 0.5 ms to 1.5 ms, similar to lifetimes found in various PL and PLE experiments [24, 33, 34, 41, 43] as well as what is expected on theoretical grounds for magnetic dipole transitions [45]. Compared to the PLE results in Ref. [24], for the seven resonances that are found in both experiments we found a shorter lifetime for each resonance, with the average difference being 250  $\mu$ s. This reduction in lifetime can be explained by an extra non-radiative mechanism in our crystal, activated by the different geometry or sample parameters.

The distribution of lifetime fits and standard errors [Fig. 4(b)] does not show separated groups with equal lifetimes, thus it is difficult to associate different peaks within the same site based on the lifetime alone.

## DISCUSSION

In photonic cavities, the maximum Purcell factor  $F = 2g/(\gamma_{\text{bulk}})$  is determined by the optical transition-cavity mode coupling strength  $g$  and is achieved for the cavity mode damping rate, i.e. at the transition between weak and strong coupling regimes [46]. Because of the measured sub-megahertz dephasing ( $\gamma_{\text{D}}$ ) and emission rates ( $\gamma_{\text{sp}}$ ) of the measured Er transitions, the damping rate can be reduced to  $\kappa = 4g$ . Consequently, the maximum Purcell enhancement is solely defined by the cavity design and the corresponding cavity mode volume  $V_{\text{m}} = 3\lambda^2 c / (2\pi n^3 F^2 \gamma_{\text{bulk}})$ . The 6 orders of magnitude Purcell factor required to match state-of-the-art single photon brightness [15] sets an upper bound on the cavity mode volume of  $V_{\text{m}} = 0.1(\lambda/n)^3$  assuming Er spontaneous emission rate in Si  $\gamma_{\text{bulk}} = 1$  kHz. Such an ultra-small cavity mode volume can be achieved in nanobeam Si photonic cavities [47, 48] that also provide the required quality factor  $Q = 10^5$  ( $\kappa = 2$  GHz). The homogeneous linewidth of an Er in a nanobeam cavity will be solely limited by the radiative broadening and will exceed the dephasing rate by 3 orders of magnitude making Er in Si a promising platform for carving single photon sources with state-of-the-art brightness and record single photon indistinguishability.

Various sample parameters can be investigated and optimized such as the varying the O and Er concentration, isotopically purifying Si and fine-tuning the annealing processes for the purpose of narrowing linewidths, relating to long coherence times. By reducing the O concentration for future samples, the Er-only sites can be extracted. These sites reside in higher symmetry sites since the lattice is undisturbed by the O. Likewise, for Er-O complexes, the inhomogeneity in the environment is affected at different O concentrations and thus could alter the linewidths.

The current signal-to-noise ratio (SNR) of the PLE spectrum suggests that the Er concentration can be diminished by up to two orders of magnitude without increasing the repetition number to detect the resonances. A reduced ion concentration leads to less ion-ion interactions, potentially narrowing the homogeneous linewidth and increasing the coherence times. Another realization to reduce inhomogeneities in the environment is to use isotopically enriched  $^{28}\text{Si}$  and by optimizing the annealing procedure.

## CONCLUSION

In this paper we use a novel in situ PLE method to study in detail the inhomogeneous linewidths and lifetimes of 70 resonances, 7 of which have been observed in Ref. [15] and 63 which have not been resolved in EPR, PL and PLE experiments before. The homogeneous linewidth of a resonance at 1538.685 nm and at 1532.254 nm were studied using transient spectral hole

burning and we extracted a homogeneous linewidth of 0.75 MHz and 1.4 MHz, respectively.

The technique presented 300 mK allows the characterization of samples on a relatively short timescale and thus measuring the dependence on the parameters discussed previously is an accessible realization. Finally, this in situ method can also be applied to optically active dopants in other thin transparent films such as  $\text{LiNbO}_3$  and  $\text{SiO}_2$ .

## ACKNOWLEDGMENTS

We acknowledge the AFAiR node of the NCRIS Heavy Ion Capability for access to ion-implantation facilities. This work was supported by the ARC Centre of Excellence for Quantum Computation and Communication Technology (Grant CE170100012) and the Discovery Project (Grant DP150103699). We thank Dr. Sae Woo Nam for kind support to establish the SSPD fabrication process at the University of New South Wales, Sydney.

## APPENDIX

### Appendix A. Detected Er resonances

Table AI: Overview table

Wavelength (nm)	Linewidth (GHz)	Lifetime (ms)	Amplitude (counts/pulse)
1539.949	2.82	1.05	0.59
1538.685 <sup>†</sup>	1.02	0.764	4.06
1538.242	1.81	0.810	1.73
1537.851	3.5	1.1	0.26
1537.652	1.95	0.70	0.57
1537.220	2.5	1.26	0.31
1536.762	0.40	0.72	1.29
1536.708	0.94	1.11	0.84
1536.687	1.5	0.97	1.13
1536.518	0.5	1.52	0.25
1536.489	1.30	1.10	0.95
1536.215 <sup>*†</sup>	1.64	0.708	2.39
1536.137	1.7	0.97	0.61
1535.899	0.83	1.19	1.40
1535.199	0.34	0.94	0.45
1534.924	4.8	0.81	0.25
1534.796	0.42	1.19	0.27
1534.672	4.7	0.88	0.57
1534.506	1.3	0.84	0.36
1534.469	3.2	0.86	0.31
1534.371 <sup>†</sup>	2.17	0.575	1.00
1534.195 <sup>*†</sup>	1.76	0.788	15.96
1534.080	1.26	1.20	1.41
1533.985	2.3	1.04	0.30
1533.885	2.08	1.48	0.80
1533.087	3.2	0.90	0.30
1532.792 <sup>†</sup>	1.6	0.49	0.41
1532.254 <sup>*†</sup>	1.208	0.682	10.63
1531.886	0.47	0.670	1.83

Table AI: (continued)

Wavelength (nm)	Linewidth (GHz)	Lifetime (ms)	Amplitude (counts/pulse)				
1530.062	1.69	1.15	0.77	1524.360*	1.09	0.578	2.41
1530.034	4.5	1.04	0.78	1523.753	3.2	1.3	0.39
1529.955	3.5	1.32	0.95	1523.535	3.8	1.11	0.85
1529.916*†	0.97	0.557	1.61	1523.126*	2.07	0.689	7.45
1529.657	1.68	0.793	3.31	1523.050	2.9	0.9	0.27
1528.380	3.9	1.14	1.53	1522.917	2.6	0.79	0.81
1527.963	3.9	0.86	0.69	1522.835	1.1	0.76	0.49
1527.851	6.9	0.97	0.41	1522.797*	0.74	0.531	2.61
1527.735	3.11	1.31	1.06	1522.399	1.0	0.82	0.24
1527.565	1.43	0.807	25.0	1522.291	3.6	0.57	0.39
1526.776	4.9	1.20	0.52	1522.114	1.0	0.8	0.19
1526.572*	1.70	0.712	3.84	1522.085	1.18	0.53	0.63
1526.171	1.74	0.93	0.69	1522.025	1.13	0.97	0.48
1526.088	1.86	1.07	1.75	1521.994	1.2	0.83	0.26
1525.885	1.8	1.03	0.24	1521.816	2.7	0.54	0.45
1525.848	3.5	0.6	0.15	1521.409	0.65	1.03	1.25
1525.751	2.9	0.98	0.29	1520.926	3.6	1.03	0.24
1525.677	1.4	1.1	0.28	1520.412	2.5	0.83	0.35
1525.513	2.8	1.56	0.32	1520.094	9.1	0.72	0.86
1524.577	2.32	1.17	3.18	1519.793	2.2	0.99	0.56
				1518.042	5.3	1.15	0.61

† Observed in Ref. [24].

\* Biexponential decay.

- [1] C. W. Thiel, T. Böttger, and R. L. Cone, *Journal of Luminescence* **131**, 353 (2011).
- [2] T. Böttger, C. W. Thiel, R. L. Cone, and Y. Sun, *Phys. Rev. B* **79**, 10.1103/PhysRevB.79.115104 (2009).
- [3] M. J. Zhong, M. P. Hedges, R. L. Ahlefeldt, J. G. Bartholomew, S. E. Beavan, S. M. Wittig, J. J. Longdell, and M. J. Sellars, *Nature* **517**, 177 (2015).
- [4] M. Rančić, M. P. Hedges, R. L. Ahlefeldt, and M. J. Sellars, *Nature Physics* **14**, 50 (2017).
- [5] R. Kolesov, K. Xia, R. Reuter, R. Stohr, A. Zappe, J. Meijer, P. R. Hemmer, and J. Wrachtrup, *Nature Communications* **3**, 10.1038/ncomms2034 (2012).
- [6] P. Siyushev, K. Xia, R. Reuter, M. Jamali, N. Zhao, N. Yang, C. Duan, N. Kukharchyk, A. D. Wieck, R. Kolesov, and J. Wrachtrup, *Nature Communications* **5**, 10.1038/ncomms4895 (2014).
- [7] J. M. Kindem, A. Ruskuc, J. G. Bartholomew, J. Rochman, Y. Q. Huan, and A. Faraon, *Nature* **580**, 201 (2020).
- [8] M. Raha, S. Chen, C. M. Phenicie, S. Ourari, A. M. Dibos, and J. D. Thompson, *Nature Communications* **11**, 1605 (2020).
- [9] S. Chen, M. Raha, C. M. Phenicie, S. Ourari, and J. D. Thompson, *Science* **370**, 592 (2020).
- [10] T. Utikal, E. Eichhammer, L. Petersen, A. Renn, S. Goetzinger, and V. Sandoghdar, *Nature Communications* **5**, 10.1038/ncomms4627 (2014).
- [11] C. Yin, M. Rančić, G. G. de Boo, N. Stavrias, J. C. McCallum, M. J. Sellars, and S. Rogge, *Nature* **497**, 91 (2013).
- [12] T. Zhong, J. M. Kindem, J. G. Bartholomew, J. Rochman, I. Craiciu, E. Miyazono, M. Bettinelli, E. Cavalli, V. Verma, S. W. Nam, F. Marsili, M. D. Shaw, A. D. Beyer, and A. Faraon, *Science* **357**, 1392 (2017).
- [13] M. Grimm, A. Beckert, G. Aeppli, and M. Müller, *PRX Quantum* **2**, 010312 (2021).
- [14] A. J. Kenyon, *Semiconductor Science and Technology* **20**, R65 (2005).
- [15] L. Weiss, A. Gritsch, B. Merkel, and A. Reiserer, *Optica* **8**, 40 (2021).
- [16] M. Steger, K. Saedi, M. L. W. Thewalt, J. J. L. Morton, H. Riemann, N. V. Abrosimov, P. Becker, and H. J. Pohl, *Science* **336**, 1280 (2012).
- [17] J. T. Muhonen, J. P. Dehollain, A. Laucht, F. E. Hudson, R. Kalra, T. Sekiguchi, K. M. Itoh, D. N. Jamieson, J. C. McCallum, A. S. Dzurak, and A. Morello, *Nature Nanotechnology* **9**, 986 (2014).
- [18] L. Bergeron, C. Chartrand, A. T. K. Kurkjian, K. J. Morse, H. Riemann, N. V. Abrosimov, P. Becker, H. J. Pohl, M. L. W. Thewalt, and S. Simmons, *PRX Quantum* **1**, 020301 (2020).
- [19] A. Yang, M. Steger, T. Sekiguchi, M. L. W. Thewalt, J. W. Ager, and E. E. Haller, *Applied Physics Letters* **95**, 10.1063/1.3238268 (2009).
- [20] H. Przybylińska, W. Jantsch, Y. Suprun-Belevitch, M. Stepikhova, L. Palmethofer, G. Hendorfer, A. Kozaneccki, R. J. Wilson, and B. J. Sealy, *Physical Review B* **54**, 2532 (1996).
- [21] R. A. Hogg, K. Takahei, and A. Taguchi, *Journal of Applied Physics* **79**, 8682 (1996).
- [22] J. Palm, F. Gan, B. Zheng, J. Michel, and L. C. Kimerling, *Phys Rev B Condens Matter* **54**, 17603 (1996).
- [23] K. Takahei and A. Taguchi, *Journal of Applied Physics* **77**, 1735 (1995).
- [24] L. Weiss, A. Gritsch, B. Merkel, and A. Reiserer, *ArXiv* (2020).
- [25] G. G. de Boo, C. Yin, M. Rančić, B. C. Johnson, J. C. McCallum, M. J. Sellars, and S. Rogge, *Phys. Rev. B* **102**, 155309 (2020).

- [26] J. L. Benton, J. Michel, L. C. Kimerling, D. C. Jacobson, Y. H. Xie, D. J. Eaglesham, E. A. Fitzgerald, and J. M. Poate, *Journal of Applied Physics* **70**, 2667 (1991).
- [27] S. Coffa, F. Priolo, G. Franzo, V. Bellani, A. Carnera, and C. Spinella, *Physical Review B* **48**, 11782 (1993).
- [28] J. D. Carey, J. F. Donegan, R. C. Barklie, F. Priolo, G. Franzo, and S. Coffa, *Applied Physics Letters* **69**, 3854 (1996).
- [29] E. E. Wollman, V. B. Verma, A. D. Beyer, R. M. Briggs, B. Korzh, J. P. Allmaras, F. Marsili, A. E. Lita, R. P. Mirin, S. W. Nam, and M. D. Shaw, *Optics Express* **25**, 26792 (2017).
- [30] G. Gol'tsman, O. Minaeva, A. Korneev, M. Tarkhov, I. Rubtsova, A. Divochiy, I. Milostnaya, G. Chulkova, N. Kaurova, B. Voronov, D. Pan, J. Kitaygorsky, A. Cross, A. Pearlman, I. Komissarov, W. Slysz, M. Wegrzecki, P. Grabiec, and R. Sobolewski, *Ieee Transactions on Applied Superconductivity* **17**, 246 (2007).
- [31] F. Marsili, F. Bellei, F. Najafi, A. E. Dane, E. A. Dauler, R. J. Molnar, and K. K. Berggren, *Nano Letters* **12**, 4799 (2012).
- [32] L. Chen, D. Schwarzer, V. B. Verma, M. J. Stevens, F. Marsili, R. P. Mirin, S. W. Nam, and A. M. Wodtke, *Accounts of Chemical Research* **50**, 1400 (2017).
- [33] A. Taguchi, K. Takahei, M. Matsuoka, and S. Tohno, *Journal of Applied Physics* **84**, 4471 (1998).
- [34] F. Priolo, G. Franzo, S. Coffa, and A. Carnera, *Physical Review B* **57**, 4443 (1998).
- [35] M. Dibos, M. Raha, C. M. Phenicie, and J. D. Thompson, *Physical Review Letters* **120**, 10.1103/PhysRevLett.120.243601 (2018).
- [36] T. Böttger, Y. Sun, C. W. Thiel, and R. L. Cone, *Physical Review B* **74**, ARTN 075107 10.1103/PhysRevB.74.075107 (2006).
- [37] N. Q. Vinh, H. Przybylińska, Z. F. Krasil'nik, and T. Gregorkiewicz, *Phys. Rev. B* **70**, 10.1103/PhysRevB.70.115332 (2004).
- [38] A. Szabo, *Physical Review B* **11**, 4512 (1975).
- [39] W. E. Moerner, *Persistent Spectral Hole-Burning: Science and Applications* (Springer, 1988) p. 5.
- [40] Y. D. Huang, M. Mortier, and F. Auzel, *Optical Materials* **15**, 243 (2001).
- [41] S. Coffa, G. Franzo, F. Priolo, A. Polman, and R. Serna, *Physical Review B* **49**, 16313 (1994).
- [42] F. Priolo, G. Franzo, S. Coffa, A. Polman, S. Libertino, R. Barklie, and D. Carey, *Journal of Applied Physics* **78**, 3874 (1995).
- [43] X. Wu, R. White, U. Hommerich, F. Namavar, and A. M. CreminsCosta, *Journal of Luminescence* **71**, 13 (1997).
- [44] N. Q. Vinh, S. Minissale, B. A. Andreev, and T. Gregorkiewicz, *Journal of Physics-Condensed Matter* **17**, S2191 (2005).
- [45] C. M. Dodson and R. Zia, *Phys. Rev. B* **86**, 125102 (2012).
- [46] M. Yamaguchi, T. Asano, M. Fujita, and S. Noda, *Physica Status Solidi C - Current Topics in Solid State Physics, Vol 5, No 9* **5**, 2828 (2008).
- [47] J. Zhou, J. J. Zheng, Z. R. Fang, P. P. Xu, and A. Majumdar, *Optics Express* **27**, 30692 (2019).
- [48] R. Miura, S. Imamura, R. Ohta, A. Ishii, X. Liu, T. Shimada, S. Iwamoto, Y. Arakawa, and Y. K. Kato, *Nature Communications* **5**, ARTN 5580 10.1038/ncomms6580 (2014).
- [49] F. Marsili, V. B. Verma, J. A. Stern, S. Harrington, A. E. Lita, T. Gerrits, I. Vayshenker, B. Baek, M. D. Shaw, R. P. Mirin, and S. W. Nam, *Nature Photonics* **7**, 210 (2013).



**SUPPLEMENTAL MATERIAL: PHOTOLUMINESCENCE EXCITATION SPECTROSCOPY OF ER IN SI VIA IN-SITU SINGLE PHOTON DETECTION**

**S-A. SSPD**

The SSPD has been fabricated at the ANFF NSW-node using the technique presented in Ref. [49]. The system detection efficiency of the SSPD is obtained by calibrating the ratio between the fiber to the SSPD and the power meter. The power meter will give the theoretical value of the amount of photons  $N_{photons}$  expected on the SSPD. The system detection efficiency is then calculated using  $100\% \cdot (CR - DCR) / N_{photons}$ , where CR is the count rate when the laser is on and DCR is the dark count rate when the laser is turned off. At the bias current used for this experiment, the SSPD has a system detection efficiency of 66.27% at 1550 nm.

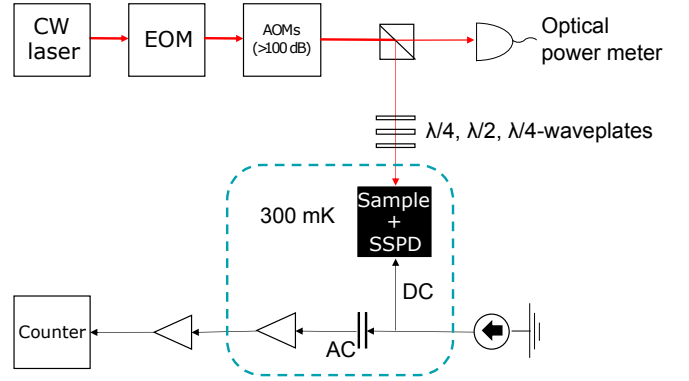


Figure S1. Experimental setup

**S-B. Photoluminescent excitation spectrum**

A schematic of the setup is shown in Fig. S1 and the in situ sample and SSPD in Fig. S2. The CW laser is the Pure Photonics PPCL550 which has been attenuated by a Thorlabs fixed attenuator (FA15T) and Thorlabs polarization maintaining variable optical attenuator (VOA50PM-APC). Afterwards, the light is split using a Thorlabs 90/10 SM beamsplitter where the low output port is connected to a Bristol 671B wavelength meter. Following the beamsplitter is a Brimrose AOM (AMM-100-10-50-1550-2FP-SM) and an AA optoelectronic AOM (MT80-IIR30-Fio-SM0) connected to their corresponding drivers which is pulsed using the Keysight 33520B with a delay between the two channels to account for the optical fibre length between the two AOMs. A Thorlabs 90/10 beamsplitter was used to direct 10% of the light to a Thorlabs PM100D power meter with an Thorlabs S154C photodiode. The higher output end is directed to polarization paddles (Thorlabs FPC031) to adjust the polarization for the magnetic field measurements.

The fiber is coupled to an Oxford HelioxVL which resides in an Oxford magnet dewar. The heliox contains the sample, SSPD, bias-tee and a homemade HEMT amplifier. The bias-tee ensures that a bias current can be applied to the SSPD and a 2 ns pulse can be read out via coaxial lines. The SSPD AC signal is amplified at room temperature using two Mini-Circuits ZFL-1000LN+. The pulse was stretched using a homemade double-comparator pulse stretcher and read out using a National Instruments 6602 counter card. The counter card was initialised to measure the number of counts in 10  $\mu$ s bins.

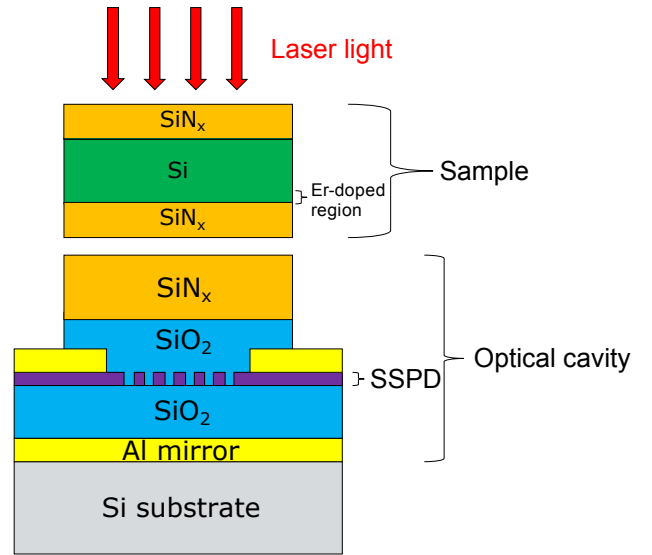


Figure S2. Sample and SSPD

**S-C. Spectral hole burning setup**

To perform the spectral hole burning measurements, polarization paddles (Thorlabs FPC032) and Covega EOM were connected in series right before the AOMs. A voltage source was connected to the DC port, a Stanford Research Systems SG384 RF source and a Keysight N512B vector source SMA outputs are combined using a Mini-Circuits RF combiner and amplified before the RF signal reaches the RF port of the EOM. The SRS SG384 is set to 2.5 GHz and 0 dB m which is pulse triggered by an external pulse. The Keysight N512B is set to  $(2.5 + \Delta f)$  GHz where  $\Delta f$  is the detuning frequency, additionally the vector source is triggered on its internal clock, which is triggered externally. To pulse both RF sources externally, a BNC T-piece was connected to the sync output of the Keysight 33520B used to pulse the AOMs. One end was directly coupled to the external

pulse input on the Keysight N512B and an internal delay is set to output the RF pulse after the trailing edge of the SRS SG384 pulse. The other end of the T-piece is connected to the external input of a Keysight 33511B, which outputs an inverted pulse signal and its channel output is connected to the external input of the SRS SG384. To align the pulses, delays were implemented in the system which has been calibrated by coupling the fiber to the cryogenic system to a 125 MHz InGaAs photodiode, connected to Tektronix MS054 oscilloscope. The RF sources were pulsed in such a way that the SRS SG384 was continuously on except when the Keysight N512B outputs a pulse for 150  $\mu$ s, where the last 50  $\mu$ s continue after the AOM extinguished the light.

The EOM was initialised by turning the RF sources off and the laser on and adjusting the DC voltage until it shows maximum extinction of the carrier. Additionally, the polarization was adjusted to extinguish the carrier further. The RF signal of the SRS SG384 is turned on to create the sidebands and the polarization is finetuned until the ratio of the optical power when the RF source is on and off is maximized. The extinction of the carrier when the RF source is on is confirmed by sweeping both sidebands over an inhomogeneous peak. The extinction ratio is over 15 dB in our spectral hole burning measurements.

The ratio between the two ends was calibrated using the PM100D power meter to calculate the amount of light on the sample. Using the calibrated detection efficiency of the SSPD, the transmission through the sample could be calculated which is estimated to be 96 %. Dividing the value by 2 gives the approximated power of one sideband on the ions.

### S-D. Lifetime measurements

The lifetimes are obtained by subtracting the offresonant time trace from a nearby onresonant time trace. A list of the chosen offresonant wavelengths is given in [SI](#).

Table SI: Overview table

Resonant wavelength (nm)	Offresonant wavelength (nm)
1539.948	1539.900
1538.685	1538.635
1538.242	1538.195
1537.847	1537.803
1537.651	1537.625
1537.219	1537.182
1536.762	1536.754
1536.708	1536.675
1536.683	1536.672
1536.517	1536.553
1536.489	1536.453
1536.215	1536.174
1536.139	1536.176
1535.899	1535.861
1535.199	1535.183
1534.925	1534.959
1534.796	1534.774
1534.673	1534.610
1534.507	1534.530
1534.469	1534.435
1534.373	1534.315
1534.194	1534.125
1534.079	1534.124

1533.984	1533.952
1533.884	1533.856
1533.090	1533.116
1532.793	1532.770
1532.254	1532.177
1531.885	1531.850
1530.063	1530.096
1530.039	1529.996
1529.958	1529.934
1529.917	1529.900
1529.656	1529.599
1528.384	1528.292
1527.960	1527.900
1527.856	1527.904
1527.738	1527.675
1527.564	1527.461
1526.774	1526.703
1526.572	1526.521
1526.170	1526.208
1526.088	1526.129
1525.885	1515.932
1525.848	1525.817
1525.750	1525.716
1525.679	1525.663
1525.514	1525.445
1524.577	1524.542
1524.360	1524.315
1523.753	1523.713
1523.532	1523.466
1523.126	1523.073
1523.052	1523.077
1522.918	1522.891
1522.834	1522.856
1522.797	1522.767
1522.400	1522.382
1522.294	1522.244
1522.113	1522.122
1522.086	1522.067
1522.025	1522.045
1521.994	1521.971
1521.817	1521.766
1521.409	1521.447
1520.926	1521.002
1520.408	1520.490
1520.097	1520.490
1519.788	1519.698
1518.042	1517.943

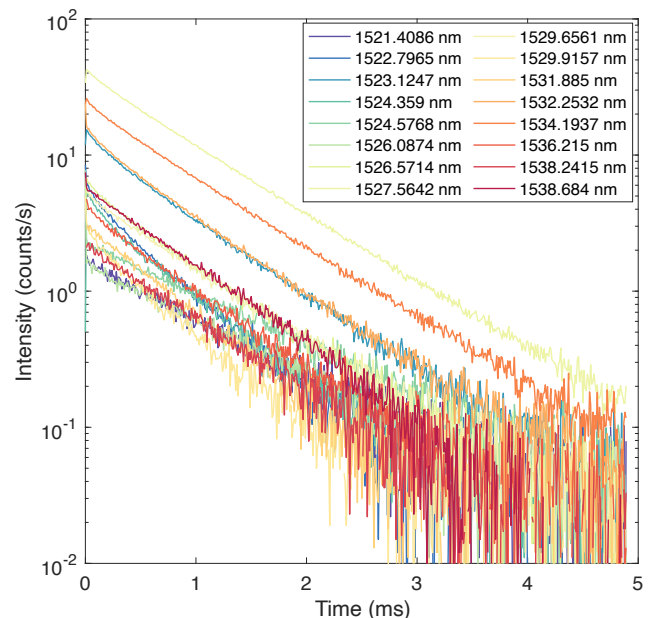


Figure S3. Photoluminescence decay for a multitude of resonances including biexponential decays.

Fig. S3 shows multiple time traces after subtracting their corresponding background.

To determine the dependence of the lifetime uncertainty on the chosen offresonant background decay, a measurement was carried out where six different background traces within ranging from  $f_0 - 2.5$  GHz to  $f_0 + 2.5$  GHz in steps of 1 GHz have been subtracted from the decay measured in the centre of the inhomogeneous peak, represented by  $f_0$ . Figure S4 shows the resulting curves for 1527.565 nm. Each trace is fitted with a single exponential and returns a lifetime and the standard error. The average of the six fitting errors is given in the column *Average fitting error* and the standard deviation in the spread of the lifetimes in column *Spread lifetimes* in table SII. This measurement was performed on a range of resonances which are presented in the column *Resonant wavelength* in table SII. Following from these 8 resonances, the choice of background trace increases the standard error on average of by 2.13.

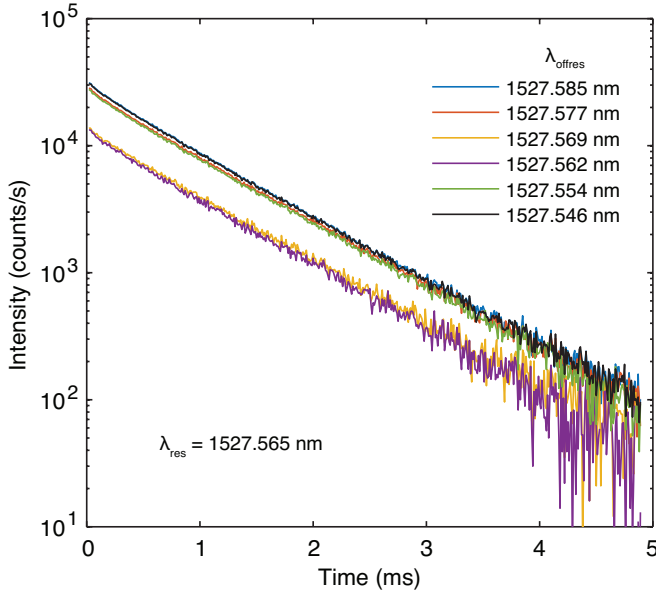


Figure S4. Photoluminescence decay with different backgrounds subtracted.

Table SII: Lifetime uncertainties

Resonant wavelength (nm)	Average fitting error ( $\mu$ s)	Spread lifetimes ( $\mu$ s)
1523.125	3.943	7.590
1527.565	2.516	6.845
1532.254	2.660	2.287
1534.194	2.235	9.540
1534.371	17.380	63.571
1536.215	15.364	18.371
1536.687	121.316	90.226
1538.685	6.442	10.859

In Fig. S5 we compare the measured decay rate (1/lifetime) to the intensity of each line to analyze if the peak height is limited by the decay rate. It is apparent from the figure that no such correlation can be drawn.

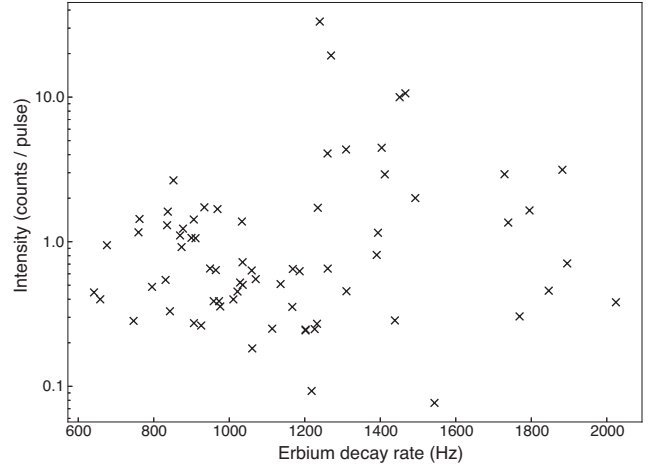


Figure S5. Intensity of each resonance as a function of the decay rate.

### S-E. Instantaneous spectral diffusion

To inspect if instantaneous spectral diffusion affects our homogeneous measurements, the spectral hole burning was performed with a  $90\ \mu\text{s}$  delay between the two pulses. The result can be seen in Fig. S6 for a pump and probe pulse of  $10\ \mu\text{s}$  each.

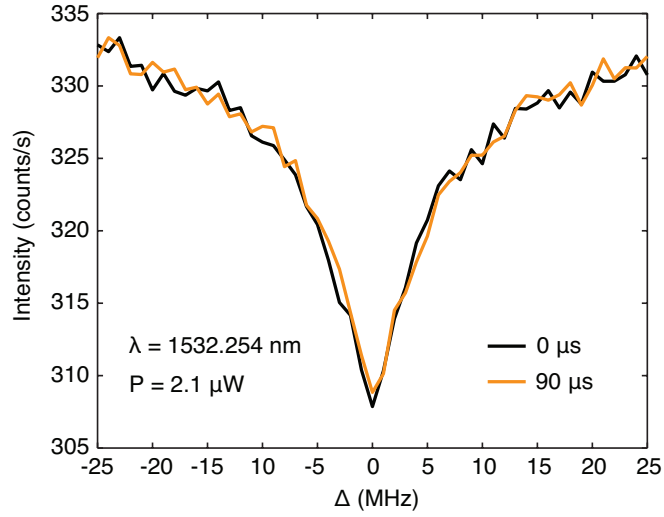


Figure S6. Overlapping plots of spectral hole burning with two different delays.